Coordinated Design of the Cartridge-type Blanket and the Ceramic Pebble Divertor for the Helical Reactor FFHR-b3

J. Miyazawa[1,2], T. Goto[1,2], Y. Hamaji[1,2], M.I. Kobayashi[1,2]

[1] National Institute for Fusion Science (NIFS), Toki, Gifu, 509-5292, Japan
[2] The Graduate University for Advanced Studies, Toki, Gifu, 509-5292, Japan

E-mail:miyazawa.junichi@nifs.ac.jp

Received xxxxxx
Accepted for publication xxxxxx
Published xxxxxx

Abstract

The cartridge-type blanket for the helical reactor has been updated and named the CARDISTRY-B3. Together with this, the ceramic pebble ergodic limiter/divertor system named the REVOLVER-D3 has been adopted in the design. There was a difficulty in fabricating the blanket cartridges due to the first wall shape with three-dimensional surface. This difficulty has been removed by introducing the slit first wall, where the first wall surface is formed by alternately stacking solid metal plates and porous plates made of metal or ceramic. The liquid metal flowing inside the blanket cartridge oozes out through the porous plates and forms the surface flow covering the first wall. Solid target plates for the helical divertor has been omitted, because the divertor region is already covered and protected by the liquid metal surface flow. The liquid metal freely falls inside the blanket cartridges by the gravity force and then exhausted to the pool set on the lower port. The ceramic pebbles, which are dropped to the inboard-side ergodic layer to form the flowing limiter divertor, also flow into the liquid metal pool. The pebbles and liquid metal are individually elevated again by screw conveyers. Since the free surface of the liquid metal is exposed to the plasma, the vapor pressure of the working liquid metal should be low enough. Ternary or quadruple alloys, which include Li, Sn, Pb (or Bi), and Er, have been selected as the candidates of the functional liquid metal for the CARDISTRY-B3 that satisfies the requirements of low vapor pressure, low density, low melting point, and high tritium breeding ratio. In this study, the coordinated design of CARDISTRY-B3 and REVOLVER-D3 for the FFHR-b3 is presented. The FFHR-b3 is one of the design options that aims at demonstration of 100 MW net electricity with two times larger devise size than LHD.

Keywords: heliotron, LHD, liquid blanket, pebble divertor, liquid metal, slit first wall

1. Introduction

Applications of the LM-PFC (Liquid Metal Plasma Facing Component) in the fusion reactor are promising from the viewpoints of high heat load tolerance and capability of self-recovering of the damage and/or the retained hydrogen. The LM-PFC applications to the divertor and/or blanket systems have been considered in the fusion reactor design for ~50 years. In typical magnetic fusion reactor designs, the divertor configuration is adopted, where the magnetic lines of force connect the fusion plasma confined inside the LCFS (Last-Closed Flux Surface) and the wall of the vacuum vessel or the blanket. For protection, the plasma contact area on the wall is

covered by an armor called the divertor target. In the fusion reactor, a divertor system including the armor and the vacuum pump is required to have a high-heat tolerability and a high particle exhaust performance to evacuate the impurities including helium ash. The blanket that surrounds the fusion plasma is one of the essential components for the DT (Deuterium-Tritium) fusion reactor having three major roles of fuel breeding, radiation shielding, and conversion of neutron kinetic energy to heat. In the blanket, tritium fuel is produced from lithium via the spallation reaction by the fusion neutrons. From the safety aspects, use of liquid metal as the working fluids of divertor or blanket is favorable, since the pressure of the liquid metal can be kept low (< 10 atm., typically) and if it leaks through the pipes or components, the liquid metal immediately becomes solidified and can be stabilized (except pure Li that is highly burnable and needs a special treatment). A high working temperature that results in a high heat efficiency can be also selectable in the blanket systems using liquid metal. As early as the early 70's, it was proposed to use the lithium flow as the divertor target in the UWMAK-I tokamak reactor design [1]. The CLiFF (Convective Liquid Flow First-wall), where the working fluid for the blanket flows on the first wall of the blanket and then to the divertor region as the droplet shower, was proposed in the ARIES-RS design [2]. In the experiment, the gallium jet-drop curtain limiter was tested on the T-3M tokamak in the early 90's [3]. Recent plasma experiments using LM-PFC are reviewed in [4].

The liquid tin shower divertor system named the REVOLVER-D (Reactor-oriented Effectively VOLumetric VERtical Divertor) has been proposed for the helical fusion reactor FFHR-d1 [5]. Melted tin was chosen as the working fluid for the REVOLVER-D, because of its low vapor pressure (< 10^{-5} Pa at 1,000 K) and low melting point (~505 K) [6]. Ten shower systems are set on the inboard side of the torus and the liquid tin shower freely falls to the inboard side of the ergodic layer surrounding the main plasma. Then, the tin shower plays a role of limiter. The neutral gas generated from recombined plasma particles can be effectively evacuated through the gaps between the tin jets. Since the free-falling liquid tin jets will have a fast velocity of ~10 m/s, it is expected to have a high heat load tolerance. On the other hand, the MHD force working on the liquid tin jets was a concern. The electric potential in the ergodic layer is complicated. If a tin jet, of which the electric resistivity is low, passes through two points with different electric potentials, a large electric current will be generated in the tin jet. The MHD force due to this electric current and the high magnetic field inside the reactor can cause a large deformation of the tin jet [7]. To avoid this, liquid tin shower has been replaced by solid tin pebble shower in the next design named the REVOLVER-D2 [8,9]. Tin pebbles are dropped to the inboard side ergodic layer and play a role of limiter. A part of tin pebbles is expected to be melted by the high heat flux inside the ergodic layer. Pebbles including melted pebbles are received in the pool set on the lower port. This pool is filled with melted tin and all pebbles are melted inside. The liquid tin is injected into a silicon oil pool as the droplet shower. The droplets become solidified and pebbles are reproduced. These pebbles are transported to the top of the reactor by a screw conveyer and then circulated again. The difficulty of the REVOLVER-D2 is in the formation process of solid tin pebbles. Instead of tin pebbles, ceramic pebbles are adopted in the new design as is discussed below. The multi-layered ceramic pebble divertor concept was intensively studied in Osaka Univ. in the early 2000s [10-13]. The cascading pebble divertor using W-coated SiC pebbles or W-coated graphite pebbles was adopted in the conceptual design of an STPP (Spherical Tokamak Power Plant) [14] and an ST-based CTF [15]. More recently, the ferromagnetic pebble divertor concept was proposed by Gierce and the FZJ group [16]. Our proposal can be distinguished from these former studies in that the REVOLVER-D3 will employ pure ceramic pebbles of SiC or other.

Advanced blanket systems using molten salt or liquid metal have been considered in the long FFHR design activity since 1994 [17-19]. To make construction and maintenance easier, toroidally separated blanket systems named the T-SHELL blanket was proposed [20]. This concept was then improved to the CARDISTRY-B (CARtridges Divided and InSerTed RadiallY - Blanket) [21]. The CARDISTRY-B is compatible with the REVOLVER-D. However, there were several issues. The blanket cartridges of the CARDISTRY-B were toroidally segmented every two degrees. As a result, the number of cartridges was large. Due to the slanted shapes, it was difficult to manufacture the cartridges. In the FFHR series, the main plasma has the shape of a rotating ellipsoid, and four magnetic fluxes called divertor legs, two each from the elliptical major axis side, extend to the divertor target region. This is called the helical divertor configuration. Low compatibility with the helical divertor and necessity of extremely large bellows for large maintenance ports were also the concerns. To solve these issues, an improved design named the CARDISTRY-B2 was proposed [22]. The adjoining cartridges were combined to form a block-type cartridge. The manufacturability has been largely improved and the number of cartridges is roughly halved. The helical divertor unit is set on each cartridge. It becomes possible to install the tangential port for the NBI (Neutral Beam Injection) heating according to the necessity. Extremely large bellows are not necessary because the cryostat for the SC (Super Conducting) magnet coils is formed by the shielding blanket cartridges inside the VV (Vacuum Vessel). To minimize the space between the first wall of the cartridge and the plasma, three-dimensional shape has been adopted in the design of the CARDISTRY-B2. On the other hand, the three-dimensional shape makes manufacturing of the cartridges difficult. This has been the last issue of the cartridge blanket design. As will be discussed below, this

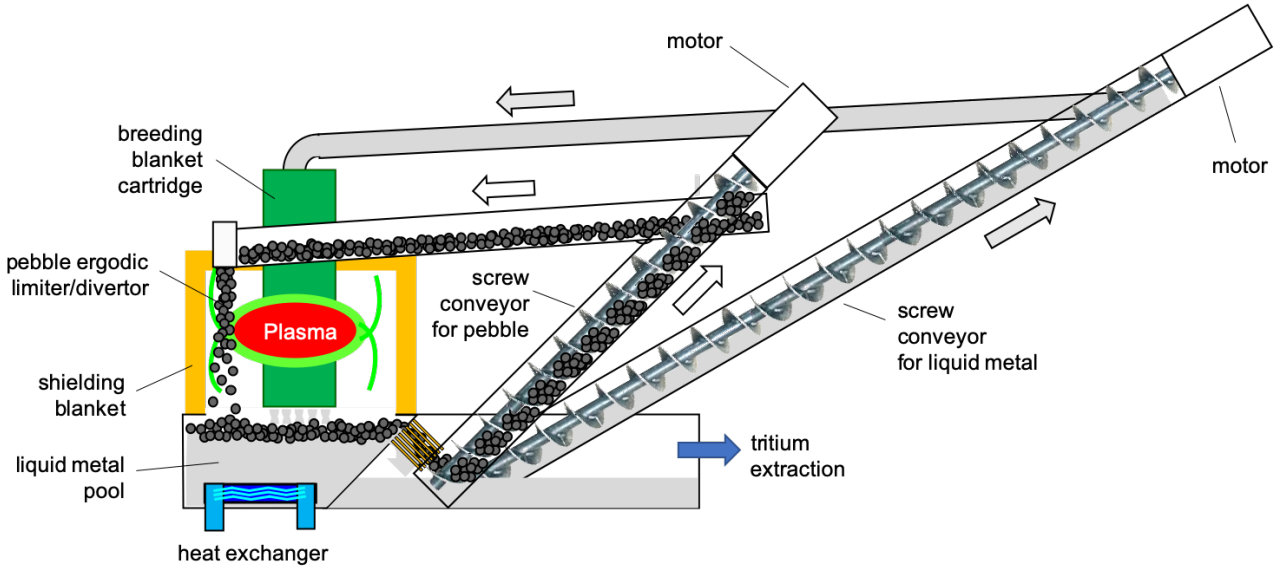

Figure 1. Schematic view of the REVOLVER-D3 for the FFHR-b3.

difficulty has been removed by introducing the slit first wall in the design.

There are several requirements on the working fluid of the new cartridge-type blanket. For example, the vapor pressure at the working temperature of ~500°C should be low enough, since the free surface of the liquid metal is exposed to the plasma. At the same time, the TBR (Tritium Breeding Ratio) should be high enough. Low density is favorable to reduce the pump power. A good compatibility with the blanket material is also required. To find the FLM (Functional Liquid Metal) that can satisfy these requirements, a basic study has been started. Several ternary or quaternary alloys, which include Li, Sn, Pb (or Bi), and Er, are selected as the candidates of FLM, as will be discussed later. The initial result of the corrosion test using one of the candidates of FLM will be also given.

In this paper, improved designs of pebble divertor and cartridge-type blanket are described. The design target is set on the FFHR-b3, which is recently defined by taking the confinement enhancement due to the magnetic configuration optimization into account [23]. The device parameters of the FFHR-b3 is given in the next section. The new pebble divertor concept is described in Section 3. The new cartridge-type blanket concept with slit first wall is described in Section 4. Details of the FLM as the working fluid for the new cartridge-type blanket and the results of an initial experiment are given in Section 5. Finally, these are summarized in Section 6.

2. Device parameters of the FFHR-b3

The FFHR-b3 is the newly defined design option of the FFHR series in the step-by-step development strategy [24]. The main objective of the FFHR-b3 is to demonstrate 100 MW net electricity in steady-state with the device size as small as possible. The plasma parameter of the FFHR-b3 has been determined by taking the confinement improvement factor of 1.3 compared with the data obtained in the LHD (Large Helical Device [25]) into account [23]. The device size of the FFHR-b3 finally determined is two times larger than the LHD. The major radius of the helical coils, R_c, is 7.8 m, and the magnetic field strength, B_c, at R_c is 6.6 T. The fusion power, P_{fusion}, of 340 MW will be sustained with the alpha heating power, P_α, of 68 (= 340 × 1/5) MW and the auxiliary heating power, P_{aux}, of 30 MW. The gross electricity, P_{gross}, and the net electricity, P_{net}, are 183 MW and 106 MW, respectively. Both the central temperature of ions, T_{i0}, and electrons, T_{e0}, will be 10 keV, at the central electron density, n_{e0}, of 3.3×10^{20} m^{-3}, and the central beta, β_0, of 5 %.

It is also estimated that the averaged heat load on the helical divertor, $\langle \Gamma_{HD} \rangle$, will be 6.3 MW/m^2. It should be noted that this $\langle \Gamma_{HD} \rangle$ is estimated for the case without the pebble divertor. In this study, 70 % of the divertor heat load is assumed to be absorbed by the pebble divertor and the rest of 30 % goes to the helical divertor, as in the former studies [8,9]. With the pebble divertor, $\langle \Gamma_{HD} \rangle$ can be reduced to 6.3 × 0.3 ~ 1.9 MW/m^2. Assuming that the radiation loss, P_{rad}, is 30 % of $P_\alpha + P_{aux}$, the total heat load on the pebble divertor is (68 + 30) × 0.7 ~ 69 MW. In Ref. 5, the plasma wetted area on the one side of the tin shower was estimated to be 0.5 × 1.0 × 0.25 = 0.125 m^2, in the case of the FFHR-d1, of which the device size is four times larger than the LHD. In the ergodic layer, the plasma hits the front and back of ten showers, *i.e.*, the total plasma wetted area on the showers is 0.125 × 20 = 2.5 m^2 in the FFHR-d1. Since the pebble flow will have a similar geometry as the tin shower, the total wetted area on the pebble flow in the FFHR-b3 is estimated to be 2.5 × (2.0/4.0)^2 ~ 0.625 m^2. Finally, the averaged heat load on the pebble flow is expected to be 69/0.625 ~ 110 MW/m^2. Although this is much higher than the tolerable heat load for the conventional tungsten divertor, there is a

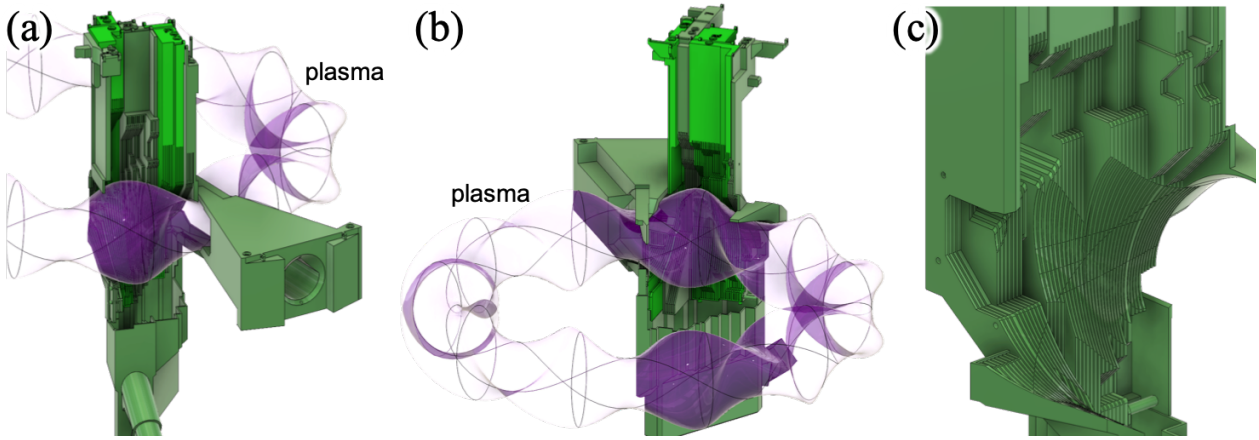

Figure 2. Schematic views of the breeding blanket cartridges of the CARDISTRY-B3 on (a) the inboard side and (b) the outboard side of the torus. (c) An enlarged view of the breeding blanket cartridges on the outboard side.

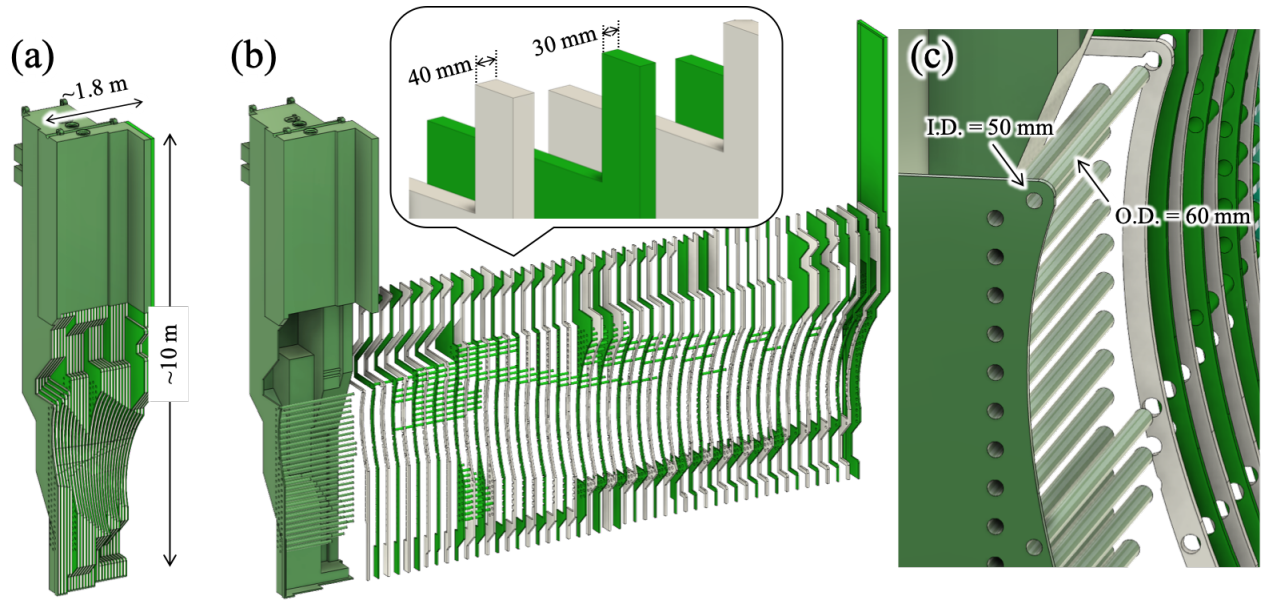

Figure 3. (a) Breeding blanket cartridge, BB09, of the CARDISTRY-B3 designed for the FFHR-b3. (b) Exploded view of the BB09. (c) Enlarged view of the horizontal hollow bars.

possibility that the pebble divertor can manage the high heat load. Further discussion on this will be given in the next section.

3. REVOLVER-D3

A schematic view of the REVOLVER-D3 is depicted in Fig. 1. The basic scenario is the same as those of former REVOLVER-D and REVOLVER-D2. Pebbles are dropped from the ten pebble droppers set on the inboard side of the torus to the ergodic layer. As the liquid tin shower in the REVOLVER-D, pebbles play a role of limiter. Pebbles flow into the pool set on the lower port, where liquid metal exhausted from the blanket cartridges is stored. The liquid metal absorbs the drop impact of the pebbles. The high temperature pebbles heated by the plasma are cooled in the liquid metal pool. At this moment, it is tentatively considered that the initial temperature of pebbles is ~300°C and the temperature after plasma irradiation is more or less ~800°C. All pebbles and the liquid metal exhausted from the blanket cartridges fall into a liquid metal pool in BB13. On the other hand, the temperature of the liquid metal poured into blanket cartridges is considered to be ~300°C and it increases to ~500°C before being exhausted. The pebble that has a temperature higher than ~500°C is cooled by the liquid metal in the pool. The pebbles are then separated from the liquid metal by a filter and transported to the top of the reactor by screw conveyers. The screw conveyers will be installed on each ten sections.

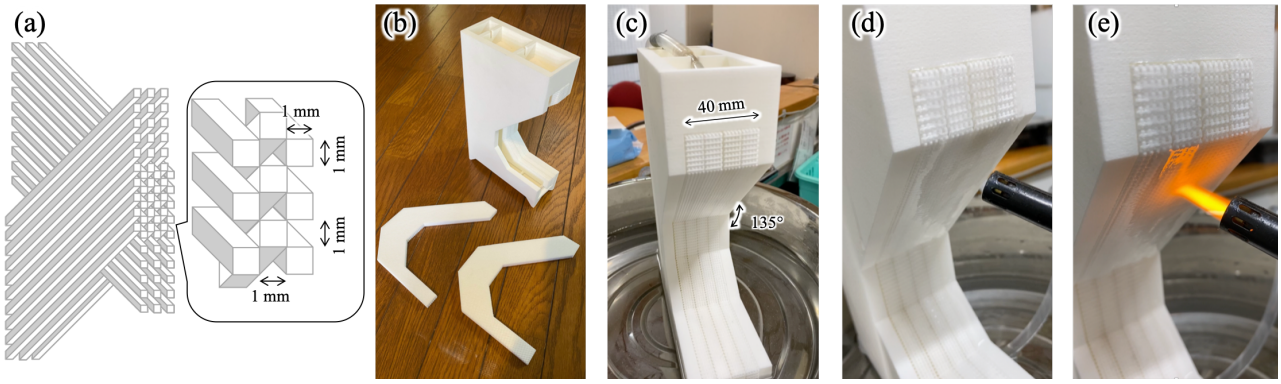

Figure 4. (a) Design of a porous material for 3D printing. (b) 3D printed porous plates. (c) A test device consisted of four porous plates. (d) Porous plates covered with the surface flow of water oozed from inside of the test device. (e) Fire resistance test of the porous plates covered by water surface flow.

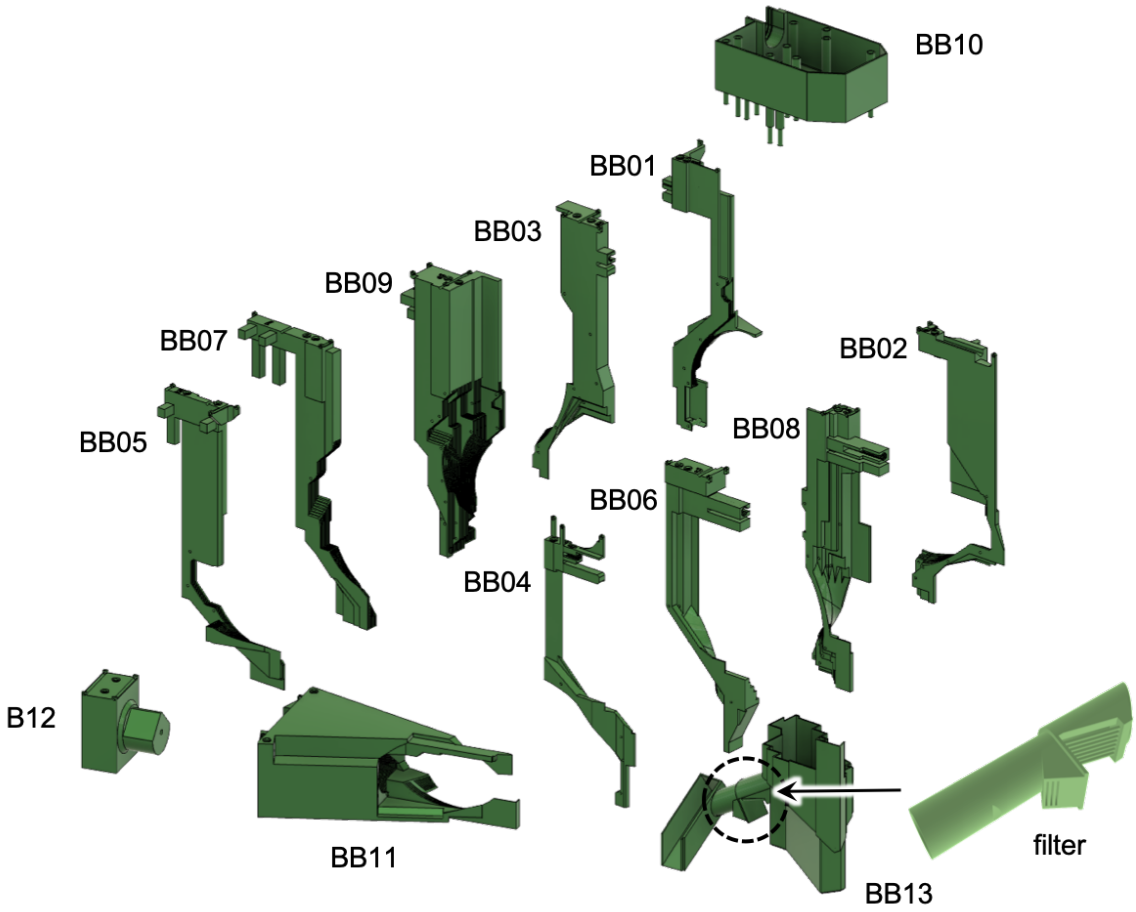

Figure 5. An exploded view of breeding blanket cartridges in a 1/10 toroidal section of the CARDISTRY-B3.

During circulation, the average temperature of the pebbles will decrease to the initial temperature of ~300°C. The liquid metal temperature of ~500°C or more in the upper region of the pool is cooled to ~300°C by a heat exchanger and then circulated again by screw conveyers. The screw conveyers for the liquid metal will be thermally insulated so that the liquid metal temperature can be kept at ~300°C during circulation. By this scenario, it becomes possible to collect the divertor heat load into the liquid metal for blanket. Pebbles transported by ten screw conveyers are stored in one place and then distributed to ten pebble droppers on each section. This scenario will be effective for keeping the redundancy of the system and for averaging the pebble flow rate in each section.

Table 1. List of volumes and weights of structure and liquid metal fully filled in the breeding blanket cartridges in one toroidal section of the CARDISTRY-B3 for the FFHR-b3.

Name	Volume of the structure (m^3)	Weight of the structure (ton)	Volume of liquid metal (m^3)	Weight of liquid metal (ton)	Total weight (ton)
BB01	1.98	15.9	3.17	22.2	38.1
BB02	1.97	15.8	1.97	13.8	29.6
BB03	2.04	16.3	3.55	24.9	41.2
BB04	1.07	8.6	8.15	5.7	14.3
BB05	2.06	16.5	2.20	15.4	31.9
BB06	2.57	20.6	1.74	12.2	32.7
BB07	3.02	24.1	4.20	29.4	53.6
BB08	3.05	24.4	2.63	18.4	42.8
BB09	5.16	41.3	1.37	95.7	137.0
BB11	11.9	95.4	21.6	151.2	246.5
BB12	1.26	10.1	8.10	56.7	66.8
Total	36.1	288.8	63.6	445.5	734.4

To separate the pebbles from the liquid metal in the pool, light pebble is favorable. This is why the ceramics as SiC or Al_2O_3 are considered as the candidate material for the pebble. The density of SiC and Al_2O_3 are ~3,100 kg/m^3 and ~3,900 kg/m^3, respectively. These are much lighter than the liquid tin (~7,000 kg/m^3) or the FLMs discussed in Section 5. From the point of view of fast temperature uniformization inside a pebble, it is preferred for the pebble material to have a high thermal diffusivity and a high specific heat. For example, the thermal diffusivities of SiC and Al_2O_3 are 7.96×10^{-5} m^2/s and 0.99×10^{-5} m^2/s, respectively, while the specific heats are 2.13×10^6 J/m^3/K and 3.04×10^6 J/m^3/K, respectively. Although the specific heat of Al_2O_3 is 1.5 times higher than that of SiC, the thermal diffusivity of Al_2O_3 is 80 times lower than that of SiC. Therefore, SiC is better than Al_2O_3 for the REVOLVER-D3.

Here, let us think a simple case with a SiC pebble of 5 mm diameter as an example. If the pebble is assumed to be dropped from 5 m above the ergodic layer, the pebble passes through the ergodic layer at ~10 m/s of velocity. The passing length inside the ergodic layer is ~0.5 m, more or less, and therefore the passing time is ~0.05 s. Then, the total heat on the pebble exposed to 110 MW/m^2 is $110 \times 10^6 \times 0.05 \times \pi \times 0.0025^2 \sim 108$ J. If we assume that this heat uniformly increases the temperature of the SiC pebble of 680 J/kg/K ~ 2.1×10^6 J/m^3/K of the specific heat, the average temperature increase is estimated to be $108 / (\times 4\pi/3 \times 0.0025^3) / (2.1 \times 10^6) \sim 786$ K ~ 500°C. However, it should be noted that the peak temperature on the pebble surface will be much higher than this simple estimation, due to the finite thermal diffusion. The peak temperature should be lower than the sublimation temperature of the SiC of ~2,500°C. This can be controlled by changing the drop distance and the pebble velocity in the ergodic layer. Simultaneous use of impurity gas puffing into the ergodic layer to increase the local radiation loss will be also effective to reduce the heat load on the pebbles. Detailed analysis and numerical simulation on the peak pebble temperature are now ongoing.

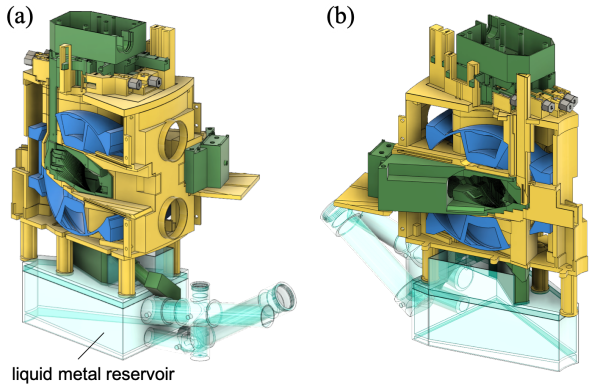

Figure 6. Bird's eye views of one toroidal section of the CARDISTRTY-B3.

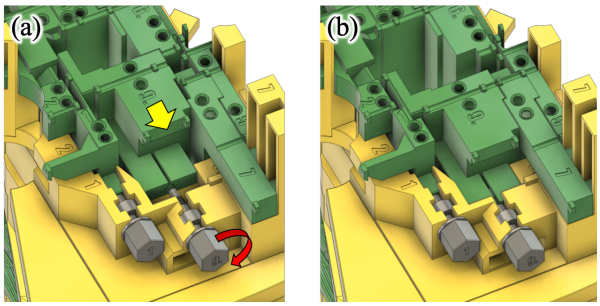

Figure 7. (a) Before and (b) after the sliding action of the BB09 by the bolt mechanism.

4. CARDISTRY-B3

Manufacturability of blanket cartridges is crucial for reduction of the construction and maintenance costs. Therefore, three-dimensional surfaces that need complicated and difficult machining process should be avoided from the design of the blanket cartridge. On the other hand, to make the full use of the

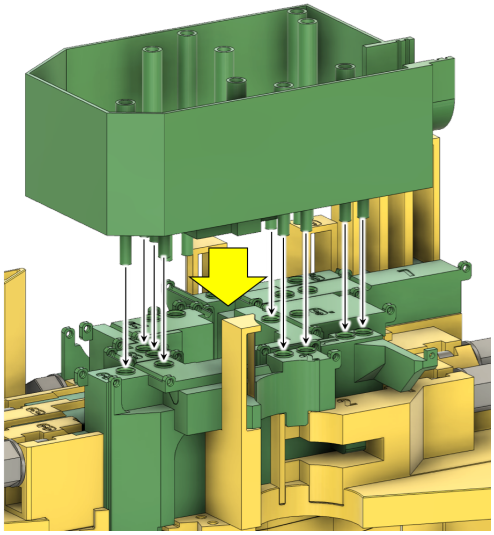

Figure 8. Installation of BB10. Injection tubes for liquid metal supply are inserted to the holes of the cartridges.

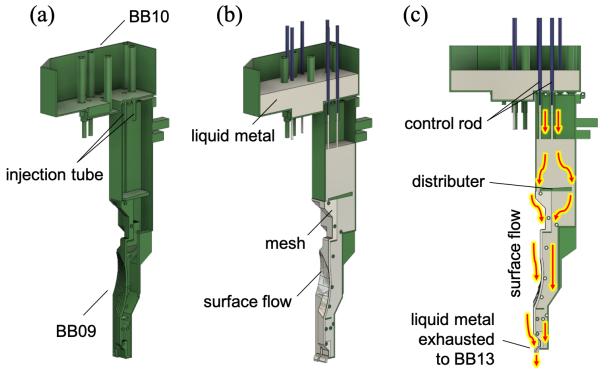

Figure 9. Sliced views of BB09 and BB10 (a) without liquid metal and (2) with liquid metal. (c) A side view of BB09 and BB10 with liquid metal. The arrows in (c) denote the liquid metal flow inside and the surface of the BB09.

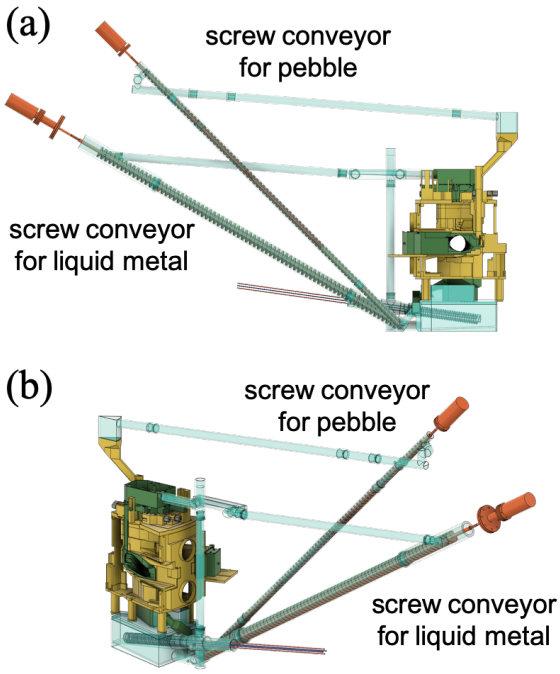

Figure 10. (a) A side view and (b) a bird's eye view of the screw conveyors for pebble and liquid metal.

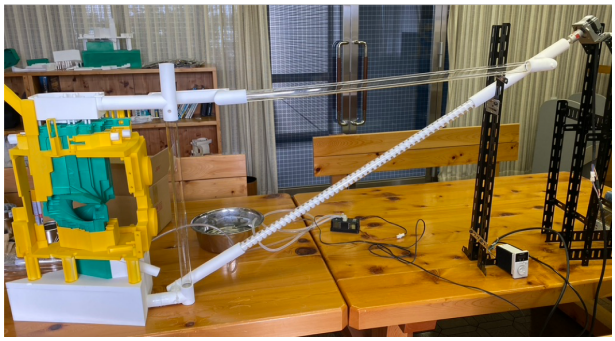

Figure 11. A reduced model of the CARDISTRY-B3 and screw conveyors for water.

space between plasma and blanket, the first wall should be three-dimensionally curved along the plasma surface. This contradiction has been solved by an idea of the slit first wall. As in a kind of three-dimensional printing, the three-dimensional surface of the first wall can be reproduced by stacking the plates cut along the first wall shape. On the other hand, it is difficult to unify the large stacked plates by welding and/or HIP (Hot Isostatic Pressing). In the slit first wall design, the plates are placed at intervals and fixed with horizontal bars. Introducing the slit first wall to the breeding blanket cartridges of the CARDISTRY-B2 [22], the CARDISTRY-B3 has been proposed. Figure 2 depicts schematic views of the blanket cartridges of the CARDISTRY-B3 with the slit first wall. The slit wall has been applied to all breeding blanket cartridges facing the plasma. Note that the tangential ports are not yet prepared in the CARDISTRY-B3, since the FFHR-b3 is adopting the ECH (Electron Cyclotron Heating) as the main auxiliary heating [23]. If necessary, it is possible to prepare the tangential ports as in the CARDISTRY-B2.

The number of slits needed to form the first wall depends on the device size. In the case of FFHR-b3, the width of a typical blanket cartridge (BB09) is ~1.8 m, as shown in Fig. 3(a). An example of slit first wall consisted of 30 mm thick solid plates and 40 mm thick porous plates are shown in Fig. 3(b). In this case, 24 solid plates and 25 porous plates are used. These plates are fixed by horizontal hollow bars of 50 mm and 60 mm of inner and outer diameters, as shown in Fig. 3(c). It is possible to fill the hollow shape with Be (beryllium) or other materials. As will be discussed in the next section, simultaneous use of FLM and Be is quite beneficial for enhancing TBR. The porous

plates can be made from 3D printed porous material or stacked meshes of metal or ceramic materials. An example of porous material made by 3D printing is shown in Fig. 4. In this case, the porous material is constructed as a mesh of 1 mm square rods arranged at 1mm intervals as in Fig. 4(a). To test the porous plates, a test device that mimics the slit first wall has been manufactured (Figs. 4(b) and 4(c)). When water was supplied from the top of the test device, water oozed through the porous material and a surface flow of water was formed (Fig. 4(d)). In this test device, a part of the first wall is slanted 45 degrees from the horizontal plane. Even in this slanted plane, the water did not drip from the surface. The water surface flow can protect the test device from fire, as shown in Fig. 4(e).

An exploded view of the breeding blanket cartridges in a 1/10 toroidal section of the CARDISTRY-B3 is shown in Fig. 5. The cartridges numbered from BB01 to BB09 and BB11 are equipped with the slit first wall. The BB12 is the test blanket module. Using this, it becomes possible to easily test various structural materials and tritium bleeding materials in a real rector condition. The BB10 is the upper pool that supplies liquid metal to other blanket cartridges of BB01-BB09 and BB11. The BB13 is the lower pool that temporally stores the liquid metal exhausted from the blanket cartridges. The ceramic pebbles are also stored in the BB13 and mixed with the liquid metal. After

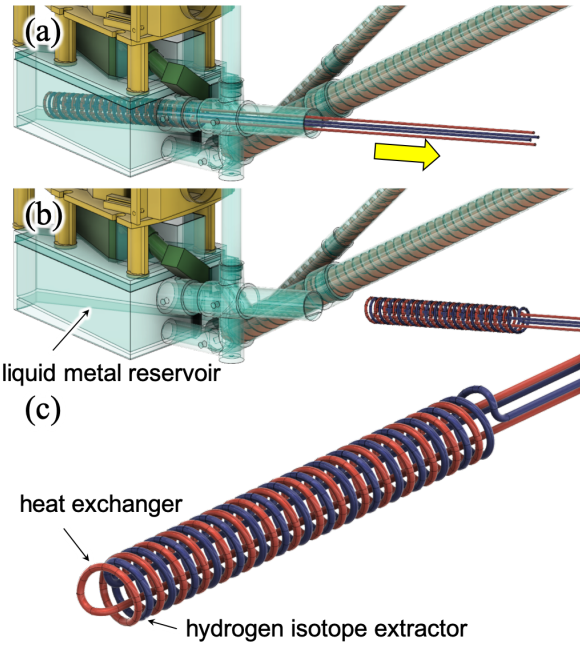

Figure 12. (a) Arrangement of the heat exchanger and hydrogen isotope extractor, (b) after being taken out for maintenance, and (c) a close-up view of it.

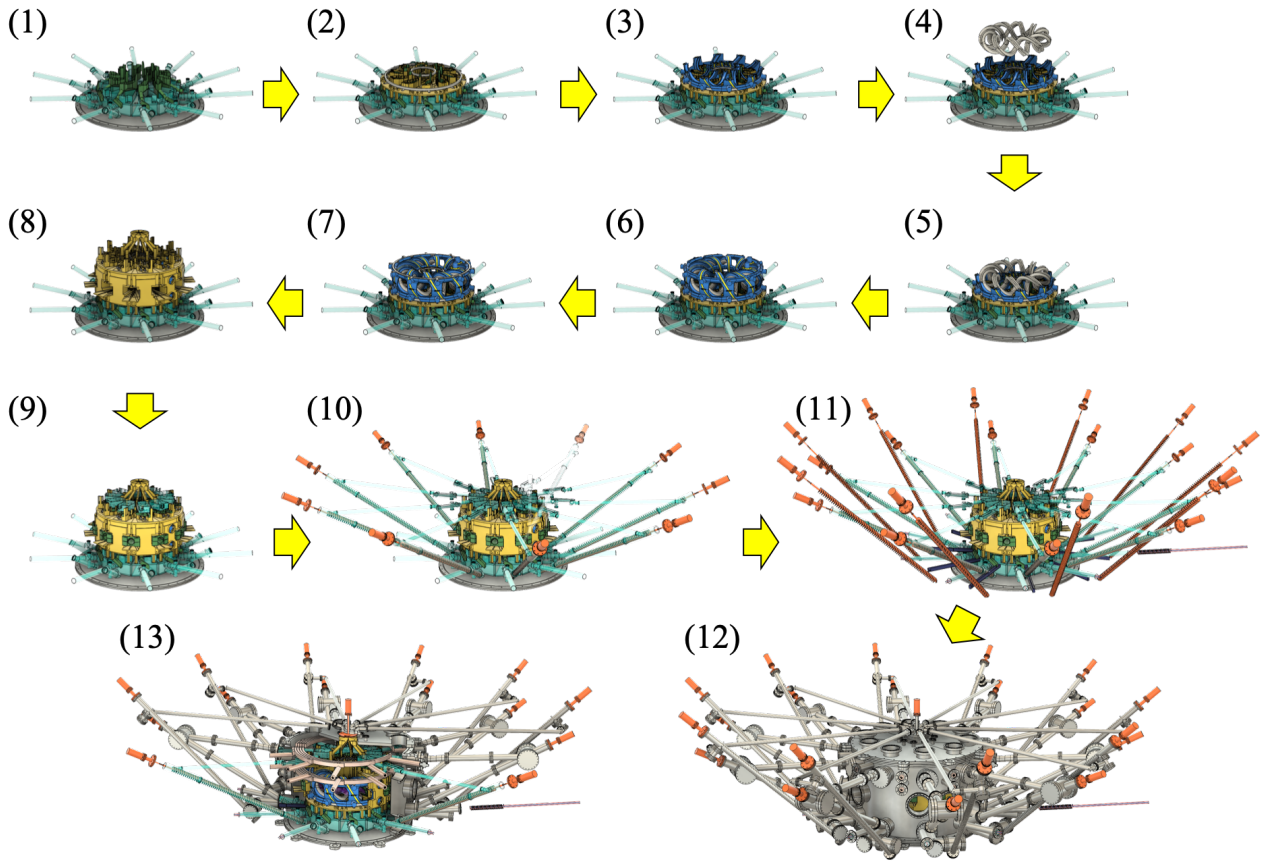

Figure 13. Schematic diagram of the construction process. See text for detailed explanation.

Table 2. Candidates of FLM for the CARDISTRY-B3. In this table, lithium is assumed to be ^{6}Li isotope enriched and composed of 90 at% of ^{6}Li and 10 at% of ^{7}Li. The liquid phase temperature and the melting point are estimated by FactSage. The vapor pressure of the FLM including Bi is a reference value obtained by assuming Pb instead of Bi, and shown in parentheses.

name	composition (at%)	density (g/cm^3)	liquid phase temperature (°C)	melting point (°C)	vapor pressure (Pa at 500°C)	TBR	neutron loss ratio
PLE-17	$Pb_{82.8}Li_{17}Er_{0.2}$	9.4	185	210	1.6×10^{-3}	1.41	0.55
PLE-25	$Pb_{74.8}Li_{25}Er_{0.2}$	8.7	186	328	1.4×10^{-3}	1.47	0.63
PLE-25 + Be	↑	↑	↑	↑	↑	1.90	0.84
BLE-25	$Bi_{74.8}Li_{25}Er_{0.2}$	8.3	252	422	(1.4×10^{-3})	1.41	0.57
BLE-25 + Be	↑	↑	↑	↑	↑	1.89	0.82
SLE-25	$Sn_{74.8}Li_{25}Er_{0.2}$	5.6	215	468	1.8×10^{-5}	1.22	0.71
SLE-25 + Be	↑	↑	↑	↑	↑	1.70	0.86
SLPE-25	$Sn_{68.8}Li_{25}Pb_6Er_{0.2}$	5.9	177	477	8.4×10^{-5}	1.25	0.71
SLPE-25 + Be	↑	↑	↑	↑	↑	1.72	0.86
SBLE-25	$Sn_{43.3}Bi_{31.5}Li_{25}Er_{0.2}$	6.9	135	599	(4.2×10^{-4})	1.30	0.67
SBLE-25 + Be	↑	↑	↑	↑	↑	1.78	0.86

the heat exchange, the pebbles are separated from the liquid metal by a filter equipped in the BB13 (see bottom right of Fig. 5). The liquid metal flows to the liquid metal reservoir set under the BB13 (Fig. 6). Crashed pebbles are separated by the filter and also goes to the liquid metal reservoir. Since the crashed pebbles float on the stored liquid metal in the reservoir, it will be not difficult to collect these at maintenance. The cartridges of BB01-BB10 are inserted from the upper port, and the BB11 and BB12 are inserted form the outer port. The BB13 is basically fixed to the lower port.

Volumes and weights of the structure and liquid metal fully filled in the blanket cartridges in one toroidal section of the CARDISTRY-B3 for the FFHR-b3 are listed in Table 1. Here, the densities of structure material and liquid metal are assumed to be 8 ton/m^3 and 7 ton/m^3, respectively. One section covers 36 degrees of the toroidal angle and therefore ten sections are needed. The total weight of BB01-B09 and BB11-BB12 including the structure and the liquid metal for all ten section is ~7,300 tons. At maintenance, all the liquid metal is drained to a reservoir (see Fig. 6). Weights of the empty cartridges ranges from 8.6 ton to 95.4 ton.

Remote maintenance of these heavy cartridges is performed by a three-point hoisting crane. Sliding action is needed to set the cartridges to the final position. Since the three-point hoisting crane is not appropriate to do this sliding action, a bolt mechanism is adopted as shown in Fig. 7. The bolt mechanism allows both push and pull motions of a cartridge. It is also possible to fix the cartridge to the final position. The sliding parts are placed on the low-dose area outside the shielding blanket. Cutting and welding of the pipes for liquid metal supply are difficult issues in the maintenance of breeding blanket. One of the largest merits of the CARDISTRY-B3 is that

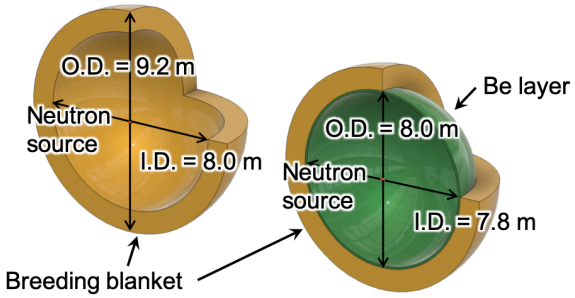

Figure 14. Spherical models with or without the Be neutron multiplier layer.

there is no piping that needs cutting and welding at maintenance. At the lower part of each cartridges, liquid metal is simply exhausted from the slit on the first wall to the pool. At the top part, on the other hand, liquid metal is supplied from the BB10 through injection tubes inserted to each cartridge, as shown in Fig. 8. The flow pattern of the liquid metal in the case of BB09 is explained in Fig. 9. The liquid metal is poured out of the BB10 through the injection tubes (Fig. 9(a)), and the BB09 is filled with the liquid metal (Fig. 9(b)). The main part of the liquid metal falls freely in BB09 by the gravity. A part of the liquid metal oozes through the meshes between the slits and the liquid metal surface flow is formed to cover the first wall (Figs. 9(b) and 9(c)). The liquid metal is finally exhausted to the BB13 under the BB09. The total flow rate in the BB09 is controlled by the control rod inserted to the injection tube. A plate is set inside the BB09 as the distributer to control the flow rates of the liquid metal flowing inside the blanket cartridge and that forming the surface flow. Detailed MHD simulation studies on

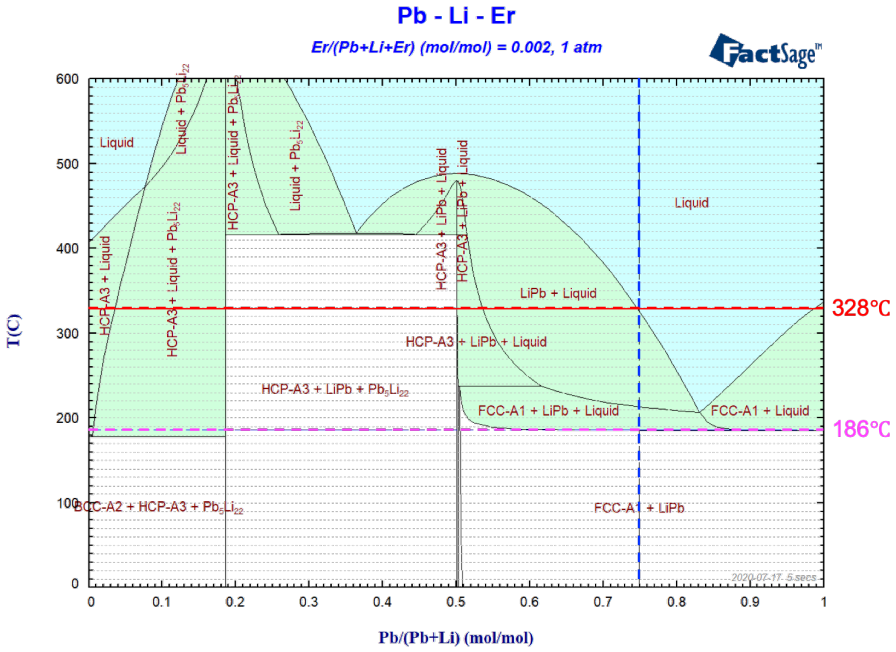

Figure 15. Phase diagram of PLE-25. Vertical dashed line denotes PLE-25 ($Pb_{74.8}Li_{25}Er_{0.2}$). Horizontal solid and dashed lines denote the liquid phase temperature and melting point, respectively.

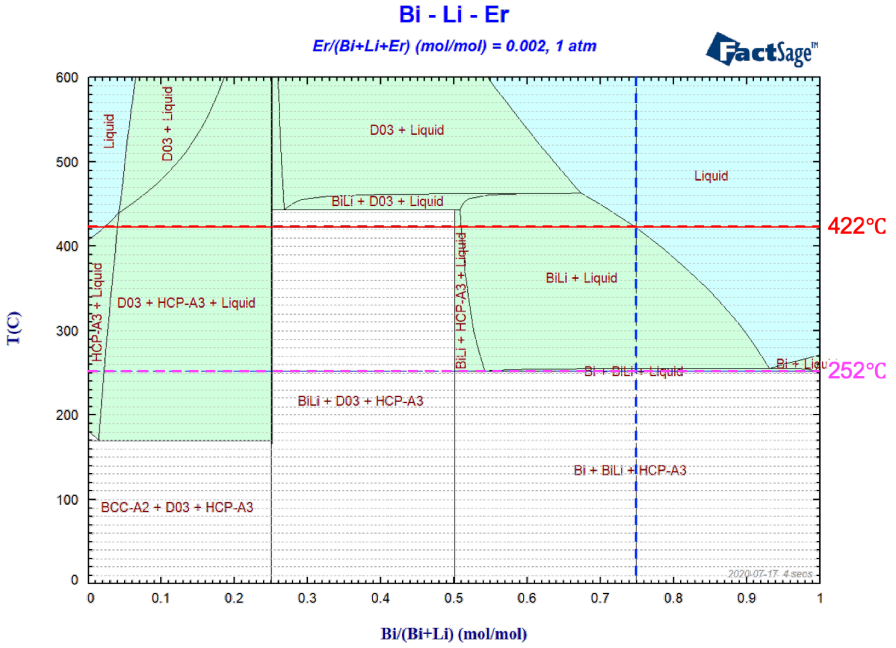

Figure 16. Phase diagram of BLE-25. Vertical dashed line denotes BLE-25 ($Bi_{74.8}Li_{25}Er_{0.2}$). Horizontal solid and dashed lines denote the liquid phase temperature and melting point, respectively.

the liquid metal flow in a strong magnetic field for all cases of BB01 to BB09, and the experiments to validate the simulation results are necessary to design the control rods and the distributers.

At each section, two screw conveyors are equipped to the liquid metal reservoir, as shown in Fig. 10. At this moment, the tilt angles of the screw conveyer for liquid metal and pebble are set to 30 degrees and 45 degrees, respectively. A large tilt angle is favorable from the point of view of space saving. To keep the screw rotation velocity low enough, on the other hand, it is necessary to set the tilt angle low [26]. The motor that drives the screw rotation is set at outside the VV and the rotation is

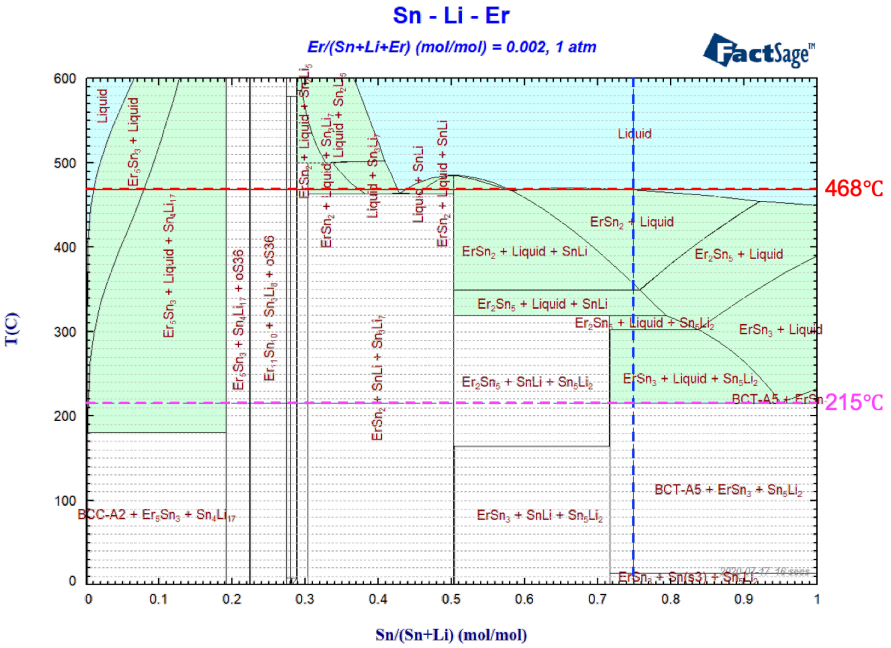

Figure 17. Phase diagram of SLE-25. Vertical dashed line denotes SLE-25 ($Sn_{74.8}Li_{25}Er_{0.2}$). Horizontal solid and dashed lines denote the liquid phase temperature and melting point, respectively.

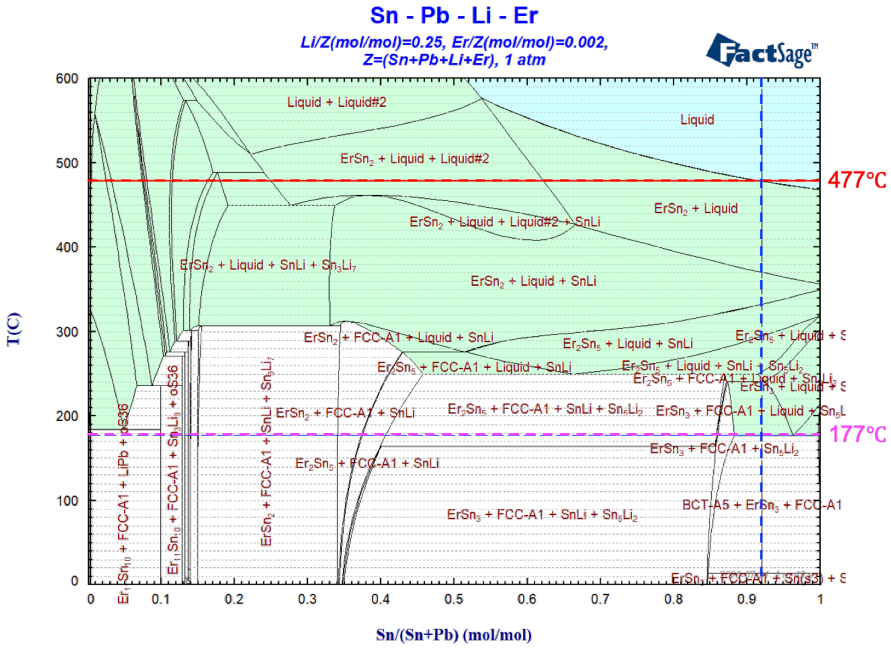

Figure 18. Phase diagram of SLPE-25. Vertical dashed line denotes SLPE-25 ($Sn_{68.8}Li_{25}Pb_6Er_{0.2}$). Horizontal solid and dashed lines denote the liquid phase temperature and melting point, respectively.

introduced inside the VV through a magnetic coupling. The magnet coupling commercially available at this moment allows the rotation velocity lower than 500 rpm (rounds per minutes). Therefore, the screw conveyor should work at a rotation velocity lower than 500 rpm. Optimization of the tilt angle for liquid and pebble is now ongoing using a reduced model as shown in Fig. 11. In the case of the screw conveyor for water in Fig. 11, of which the outer diameter of the screw is 50 mm and the tilt angle is 30 degrees, the rotation velocity of 70 rpm was enough to circulate water.

In Fig. 12(a), depicted are the heat exchanger and hydrogen isotope extractor inserted to the liquid metal reservoir.

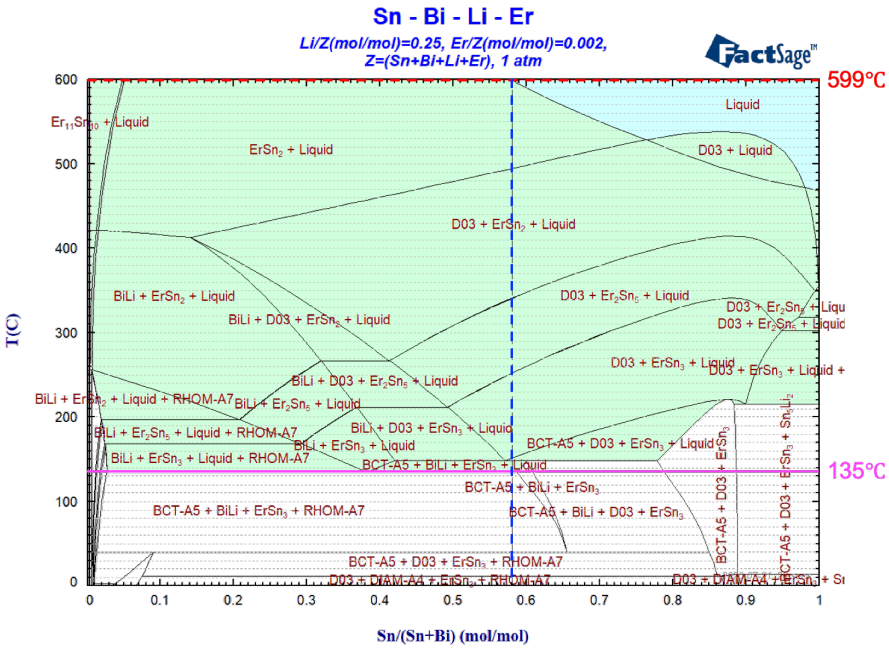

Figure 19. Phase diagram of SBLE-25. Vertical dashed line denotes SBLE-25 ($Sn_{43.3}Bi_{31.5}Li_{25}Er_{0.2}$). Horizontal solid and dashed lines denote the liquid phase temperature and melting point, respectively.

Although this design is tentative and should be considered in detail in future studies, both the heat exchanger and the hydrogen isotope extractor should be designed to be easily extracted from the device at maintenance, as shown in Fig. 12(b). To facilitate maintenance, it is effective to make the volume of the heat exchanger and the hydrogen isotope extractor as small as possible. On the other hand, the contact surface area with the liquid metal should be as large as possible. The spiral structure as depicted in Fig. 12(c) would be one of the solutions that can satisfy these contradicted requirements.

Schematic view of the construction process is depicted in Fig. 13. First of all, the liquid metal reservoir is set on the base plate (Fig. 13(1)). Then, the lower part of shielding blanket is set on the liquid metal reservoir and two planar vertical field coils are set on the shielding blanket (Fig. 13(2)). One of the two planar coils is small enough and can be installed after it is wound at another place. Another planar coil is rather large to carry. Therefore, it will be necessary to wind and complete the large planar coil on the shielding blanket. After that, the lower half of the electromagnetic support structure that tightly holds the superconducting magnet coils is installed (Fig. 13(3)). The two planar coils are fixed to the electromagnetic support structure at this timing. It will be also difficult to carry the large helical coils. The helical coils should be wound in-situ (Fig. 13(4)), as the large planar coil was. The in-situ winding method of large helical coils is now under consideration. One of the solutions is to wrap a flexible HTS (High-Temperature Superconducting) conductor around the helical coil case as if it were sewn. The WISE (Wound and Impregnated Stacked Elastic tapes) conductor [27] will be suitable for this method. After winding, the helical coil case is sealed, and low-melting-point metal is poured into the case to fix the conductor. After the two helical coils are completed on the electromagnetic support structure (Fig. 13(5)), the upper half of the electromagnetic support structure is installed (Fig. 13(6)). Then, two planar vertical field coils are set on the electromagnetic support structure (Fig. 13(7)). As in Fig. 13(2), one of the two planar coils can be installed after completed at another place, while another coil should be wound and completed in-situ. After the two planar coils are installed, the shielding blanket is installed (Fig. 13(8)). The shielding blanket is divided into several parts as in the former CARDISTRY-B2 [22], so that these can be installed after the electromagnetic support structure including four planar coils and two helical coils is completed. Then, breeding blankets (Fig. 13(9)), screw conveyors for liquid metal (Fig. 13(10)) and for pebbles (Fig. 13(11)) are installed. Finally, these are covered by the vacuum vessel and finished (Figs. 13(12) and 13(13)).

5. Functional Liquid Metal

As was already discussed in the introduction, low vapor pressure, low density, low melting point, low corrosiveness, high TBR, and high neutron shielding ability are required for the liquid metal to be used in the CARDISTRY-B3. Especially, the vapor pressure at the working temperature of ~500°C should be low enough since the free surface of the liquid metal on the first wall and/or the pool is exposed to the plasma. Based on the experiments in LHD [27], the vacuum pressure

around the divertor region of FFHR-b3 is expected to be more or less on the order of 10^{-2} – 10^{-1} Pa. The vapor pressure of the liquid metal should be kept much lower than this at the working temperature of ~500℃. In this study, we tentatively set the maximum limit of the vapor pressure of the liquid metal to be 10^{-3} Pa. A low-density liquid metal is preferable to mitigate the pump power that is given by QH/η, where Q, H, and η are the flow rate, the hydraulic head, and the pump efficiency, respectively, and Q is proportional to the density. In the case of the FFHR-b3, the pump power is considered to be ~0.8 MW assuming the liquid metal density of 5.6 g/cm^3 and the pumping efficiency of 0.6. The melting point should be as low as possible to mitigate the preheating power. Corrosiveness of the liquid metal should be also as low as possible to prolong the maintenance period of the blanket. At this moment, 1 mm/year of corrosion layer growth rate on the structure material is tentatively considered to be the maximum limit. The TBR should be larger than one. In the former study [28], TBR was evaluated for FFHR-d1 with the fully covered simple torus model and various breeders of Flibe, Flinac, Li, LiPb, and LiSn were compared. As a result, it was shown that all of these breeders can satisfy TBR > 1 in FFHR-d1. In below, we will adopt a spherical model and relatively compare the TBR for various breeders. The neutron shielding ability will be also compared relatively.

Ternary or quaternary alloys including Li, Sn, Pb (or Bi), and Er are selected as the candidates of the Functional Liquid Metal (FLM) that can satisfy the requirements. The vapor pressure of tin is quite low among the low-melting-point metals [6]. Therefore, Sn has been selected as the base material. Li is inevitable to produce tritium through a spallation reaction. Pb is added to tin to decrease the melting point and to mitigate the corrosivity of Sn. Bi can be used as the substitute substance of Pb, to avoid troublesome handling of Pb in experiments. A small amount of Er is added expecting self-formation and/or self-recovery of the oxidized Er layer that works as an anticorrosion film on the blanket materials. The attempt to form an oxidized Er layer on V (vanadium) alloys by adding a small amount of Er in liquid Li was successfully done in the past studies [30-32]. However, it has not been confirmed yet if this works for the different combinations of liquid metals and materials. Further research on this is highly required. In our case, Er is chosen as the oxidizing substances as in Refs. 30-32, since Er has much lower oxygen potential than Li [33].

Candidates of FLM for the CARDISTRY-B3 has been selected as listed in Table 2, where the names of the FLM as PLE-17, PLE-25, BLE-25, SLE-25, SLPE-25, and SBLE-25 are the abbreviation of the initials of the included materials sorted in descending order of atomic ratio and the numbers denote the atomic ratio (at%) of Li. In the table, density, liquid phase temperature, melting point, TBR, and neutron loss ratio are listed. Here, lithium is assumed to be ^{6}Li isotope enriched

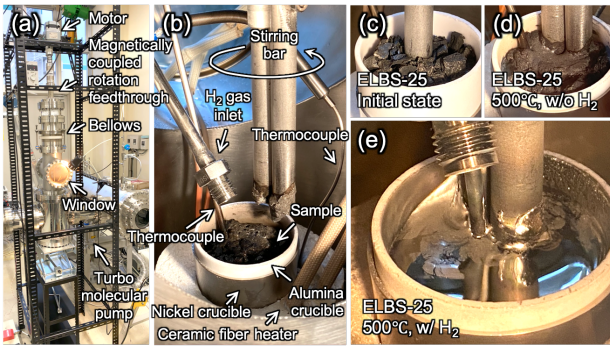

Figure 20. (a) A vacuum device used for basic experiment of FLM. (b) Internal view of the experimental device. (c) SBLE-25 in its initial state. (d) SBLE-25 heated up to 500℃ without hydrogen gas puffing. (e) SBLE-25 heated up to 500℃ with hydrogen gas puffing.

and composed of 90 at% of ^{6}Li and 10 at% of ^{7}Li. The density of a FLM, ρ_{FLM}, including N components is estimated by the following formula:

$$\rho_{\mathrm{FLM}} = \frac{\sum_{n=1}^{N} A_n \chi_n}{\sum_{n=1}^{N} A_n \chi_n / \rho_n} \tag{1}$$

where A_n, χ_n, and ρ_n denote the atomic number, the atomic ratio, and the density of the n-th atom, respectively. The liquid phase temperature denotes the lowest temperature where the liquid phase appears in the metal. The solid and liquid phases both exist at the temperature between the liquid phase temperature and the melting point. The liquid phase temperature and the melting point are calculated using the thermodynamic equilibrium calculation code FactSage. Phase diagrams of the FLMs calculated by the FactSage will be discussed later. The vapor pressure is estimated by taking the chemical activities of the compositions into account, according to the procedure of Ref. 6. At first, the vapor pressures of pure Li, Sn, and Pb are given as below.

$$p_{\mathrm{Li}} = 10.75 \times 10^9 \exp(-153{,}800 / RT), \tag{2}$$

$$p_{\mathrm{Sn}} = 65.42 \times 10^9 \exp(-309{,}200 / RT), \tag{3}$$

$$p_{\mathrm{Pb}} = 6.752 \times 10^9 \exp(-184{,}960 / RT), \tag{4}$$

where R = 8.314 J/K/mol is the gas constant and T is the temperature in K. The vapor pressure of an FLM, p_{FLM}, including N components can be expressed as below.

$$p_{\mathrm{FLM}} = \sum_{n=1}^{N} \alpha_n p_n, \tag{5}$$

where α_n and p_n denote chemical activity and vapor pressures of pure liquid atoms, respectively. The chemical activities of

Li and Sn in the case of SnLi alloy are given by

$$\alpha_{Li(SnLi)} = \exp(-19.48\chi_{Li}^3 + 21.42\chi_{Li}^2 - 1.366\,\chi_{Li} - 0.5794 + (37{,}560\chi_{Li}^3 - 48{,}310\chi_{Li}^2 + 22{,}779\chi_{Li} - 11{,}140)/T), \quad (6)$$

and

$$\alpha_{Sn(SnLi)} = \exp(-25.110\chi_{Li}^2 + 6.540\chi_{Li} - 0.5187 + (1.649\chi_{Li}^2 - 0.5931\chi_{Li} + 0.04350)/T), \quad (7)$$

respectively. On the other hand, the chemical activities of Li and Pb in the case of PbLi alloy are given by

$$\alpha_{Li(PbLi)} = \exp(-19.48\chi_{Li}^3 + 21.42\chi_{Li}^2 - 1.366\,\chi_{Li} - 0.5794 + (20{,}350\chi_{Li}^3 - 22{,}220\chi_{Li}^2 + 9{,}711\chi_{Li} - 7{,}840)/T), \quad (8)$$

and

$$\alpha_{Pb(PbLi)} = \exp(-3.291\chi_{Li}^3 + 2.044\chi_{Li}^2 - 1.755\,\chi_{Li} + 0.04122 + (652.7\chi_{Li}^3 - 1{,}270\chi_{Li}^2 + 281.6\chi_{Li} - 15.02)/T), \quad (9)$$

respectively, using the atomic ratio of Li, χ_{Li}. In this study, the chemical activities in a multi-alloy including Li, Sn, and Pb are approximated as follows.

$$\alpha_{Li(SnPbLi)} = \alpha_{Li(SnLi)} \times \chi_{Sn}/(\chi_{Pb} + \chi_{Sn}) + \alpha_{Li(PbLi)} \times \chi_{Pb}/(\chi_{Pb} + \chi_{Sn}), \quad (10)$$

$$\alpha_{Sn(SnPbLi)} = \alpha_{Sn(SnLi)} \times \chi_{Sn}/(\chi_{Pb} + \chi_{Sn}) \sim \alpha_{Sn(SnLi)} \times \chi_{Sn}/(1 - \chi_{Li}), \quad (11)$$

and

$$\alpha_{Pb(SnPbLi)} = \alpha_{Pb(PbLi)} \times \chi_{Pb}/(\chi_{Pb} + \chi_{Sn}) \sim \alpha_{Pb(PbLi)} \times \chi_{Pb}/(1 - \chi_{Li}). \quad (12)$$

In estimating the vapor pressures in Table 1, Er is neglected and Bi is assumed to have the same property as Pb. The TBR was estimated by the MCNP code [34], using a simple spherical model of 9.2 m outer diameter and 0.6 m thickness, as shown in Fig. 14. Neutrons were emitted from the point source at the center. In all cases, ^{6}Li enrichment was assumed to be 90 %. The influence of Be was checked by adding a Be layer of 0.1 m thickness on the inner surface of the blanket. The neutron loss ratio is the ratio of neutrons absorbed inside the blanket to the neutrons emitted from the neutron source, that is given by $1.0 - \Gamma_n/\Gamma_{n\_w/o\_blanket}$, where Γ_n and $\Gamma_{n\_w/o\_blanket}$ are the neutron flux on spherical surface of 4.6 m radius with and without the spherical blanket, respectively. A high neutron loss ratio means that the FLM has a high neutron shielding ability. It should be noted that the TBR and the neutron loss ratio in Table 2 should be used only for relative comparison, not for quantitative estimation. Nevertheless, we can compare our results with the simulation results using a simple torus model for FFHR-d1 in Ref. 28. If the TBR of a FLM is larger

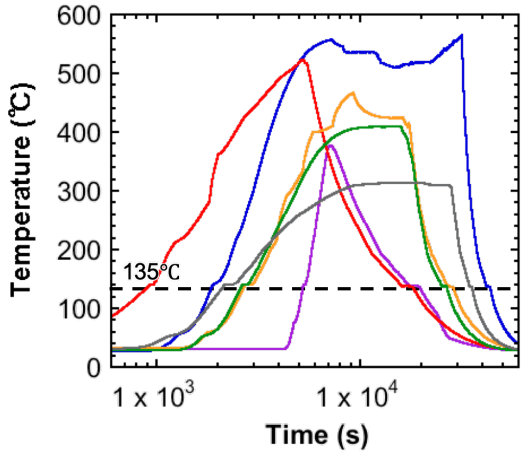

Figure 21. The history of increasing and decreasing the temperature of the SBLE-25 sample.

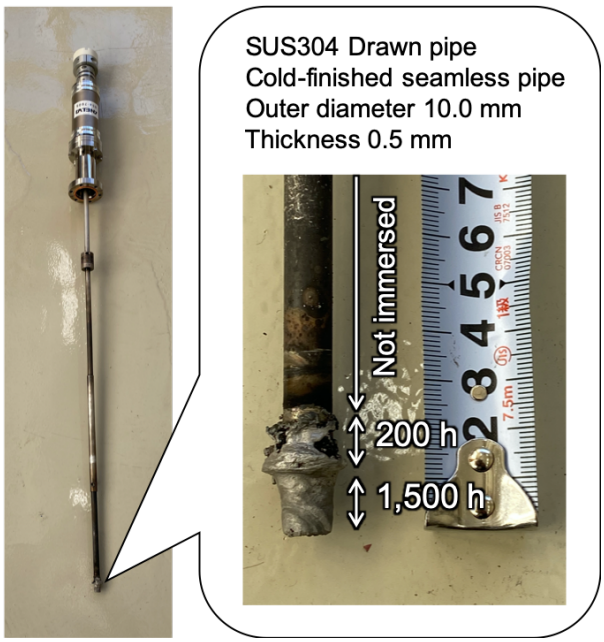

Figure 22. Overall photo and enlarged photo of the sample pipe of SUS304.

than the TBR of SLE-25 without Be of 1.22 (Table 2), then we can expect that the FLM can achieve TBR > 1 in the simple torus model for FFHR-d1, because a similar Li-Sn alloy was shown to have TBR > 1 in Ref. 28. More detailed neutron simulation coupled with the 3D-CAD data of the blanket cartridges for FFHR-b3 as in Fig. 5 are now in preparation for quantitative estimation of TBR and the neutron shielding ability. As can be seen from the differences between PLE-17 and PLE-25, both the TBR and the neutron loss ratio increase with the Li composition. In other FLMs, the composition of Li is fixed to be 25 at%, as the PLE-25. The impact of the Be layer is clearly recognized in the difference between PLE-25 and PLE-25 + Be. The TBR largely increases from 1.47 to 1.90 and the neutron loss ratio also increases from 0.63 to 0.84. Apparently, it is better to adopt the Be layer. Among the candidates of FLMs in Table 2, PLE-17, PLE-25, and BLE-25 are not necessarily suitable for the CARDISTRY-B2, because of the high vapor pressure exceeding 1×10^{-3} Pa at 500°C, although these still can be strong candidates for ordinally blanket systems using the liquid metal without exposing its free surface to the plasma. Among the remaining three candidates of SLE-25, SLPE-25, and SBLE-25, SLE-25 has the lowest density and the lowest vapor pressure of 1.8×10^{-5} Pa at 500°C. On the other hand, SBLE-25 shows the lowest liquid phase temperature of 135°C and the highest TBR of 1.78 when used with the Be layer. Although SBLE-25 including bismuth would be inadequate for the fusion reactor, because of the polonium produced by the neutron capture reaction of ^{209}Bi, it can be a good alternative of SLPE-25 in basic experiments.

Phase diagrams including PLE-25, BLE-25, SLE-25, SLPE-25, and SBLE-25 are shown in Figs. 15, 16, 17, 18, and 19, respectively. In these phase diagrams, the atomic ratios of Li and Er are fixed to 25 at% and 0.2 at%, respectively. For example, PLE-25 listed in Table 2 is expressed by the vertical broken line in Fig. 15, which denotes the atomic composition of PLE-25, *i.e.*, $Pb_{74.8}Li_{25}Er_{0.2}$, of which the atomic ratio of Pb to (Pb + Li) ~ 75 %. The liquid phase temperature and the melting point are depicted by solid and dashed horizontal lines in Figs. 15-19. The atomic compositions of SLPE-25 and SBLE-25 are determined to have a low liquid phase temperature while keeping the atomic composition of Sn as large as possible. As can be recognized in these phase diagrams, there exist various IMC (InterMetallic Compound) compositions in the solid state between the liquid phase temperature and the melting point. Therefore, these FLMs are not necessarily available to the CARDISTRY-B3 below the melting point. To check the influence of the IMC compositions on the liquified material below the melting point, a basic experiment has been carried out.

Experiments on dissolution of FLM and corrosion by FLM were tried in a vacuum device shown in Fig. 20(a). The SBLE-25 supplied by Kojundo Chemical Laboratory Co., Ltd. was used in the experiment. The measured composition ratios of Sn, Bi, Li, and Er in at% were 42.1, 30.8, 24.9, and 2.2, respectively. Compared with the requested composition of $Sn_{43.3}Bi_{31.5}Li_{25}Er_{0.2}$, the composition ratio was well reproduced. Although the composition ratio of Er is ten times larger than the requested value, the phase diagram scarcely changes with this difference. The sample of SBLE-25 was put in an alumina crucible set inside a nickel crucible as shown in Fig. 20(b). A ceramic fiber heater was used to heat the crucibles. Thermocouples were put into the heater and the sample. In the initial state, the SBLE-25 looks like black grains of coal (Fig. 20(c)). Even after the temperature was increased, the SBLE-25 was still black and highly viscous (Fig. 20(d)). Although the pressure inside the experimental device was on the order of 10^{-4} Pa, the SBLE-25 was apparently oxidized. When reduction was attempted by introducing a small amount of hydrogen gas at a rate of 5 – 10 sccm, a metallic luster was obtained within a few minutes and the viscosity was decreased (Fig. 20(e)). Since the plasma confinement region is filled with hydrogen isotopes, this reduction effect can be expected also in a fusion reactor. The history of increasing and decreasing the temperature of the sample for several times is shown in Fig. 21. The temperature

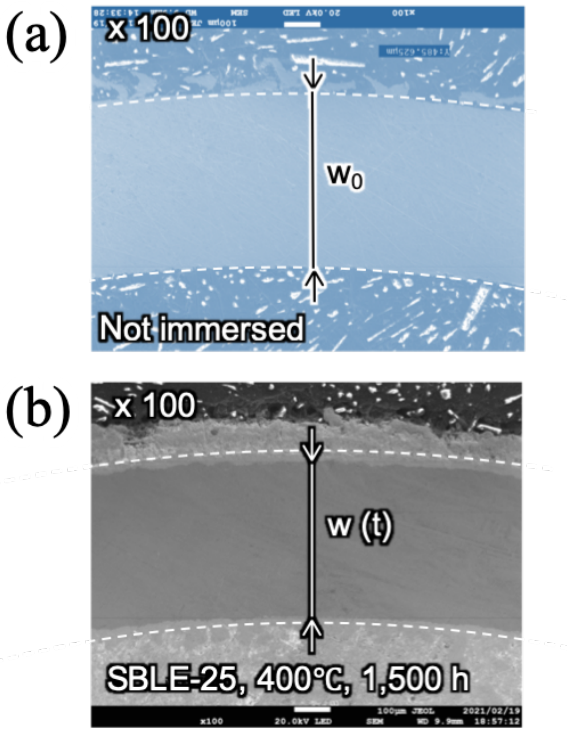

Figure 23. SEM images of the sample pipe sliced at (a) a part not immersed in SBLE-25, and (b) a part immersed in SBLE-25 at 400°C for 1,500 hours. White broken curves denote the initial positions of outer and inner edges of the sample pipe.

stagnated both increase and decrease, forming a plateau at ~135°C. These results indicate the liquid phase temperature of SBLE-25 is ~135°C, as expected in Fig. 19.

As shown in Fig. 20, it is possible to insert one or two pipes into the SBLE-25 in the crucible. These pipes can be rotated by a motor connected by a magnetically coupled rotation feedthrough. Using this mechanism, an initial trial of corrosion test has been carried out. In this experiment, a drawn cold-finished seamless pipe of SUS304 was used as the test material. The outer diameter and the thickness of the pipe was 10.0 mm and 0.5 mm, respectively. The pipe was inserted to SBLE-25 heated to 400°C in a vacuum of the order of 10^{-4} Pa. For reduction, H_2 gas was puffed to SBLE-25 through the gas inlet shown in Fig. 20(b), at a rate of 5 sccm. Even at 400°C, the metallic luster of SBLE-25 was kept and the viscosity seemed not largely changed compared with that at 500°C shown in Fig. 20(e). The pipe was rotated at 50 rpm or slower. Due to some axial shaking, the pipe moved along the inner edge of the crucible and stirred the inside. For first 200 hours, the pipe was inserted to SBLE-25 for ~20 mm. After 200 hours, the pipe was vertically extruded for ~10 mm. Then, the corrosion experiment was continued for more 1,300 hours. As a result, the pipe was immersed to SBLE-25 for 1,500 hours from the tip to 10 mm, and for 200 hours from 10 mm to 20 mm from the tip (Fig. 22).

The pipe was then cut and investigated by SEM (Scanning Electron Microscope) and EDX (Energy Dispersive X-ray Spectrometer) of JSM-7100F. SEM images of the sample pipe sliced at a part that was not immersed in SBLE-25, and a part that was immersed in SBLE-25 at 400°C for 1,500 hours are shown in Figs. 23(a) and 23(b), respectively. After immersion in SBLE-25 for 1,500 hours, the thickness of the pipe apparently reduces from the initial value of $w_0 = 0.5$ mm. This is due to the formation of IMC layer. This means that the oxidized layer of Er that works as an anticorrosion film was not self-formed, unfortunately. In a previous study using V, self-formation of Er oxide layer was observed when V was pre-oxidized [30-32]. In our case, SUS304 was not pre-oxidized and did not contain a large amount of oxygen as V. Even though self-formation did not occur, there still is a possibility of self-recovery of the Er oxide layer by the Er in FLM. Further corrosion experiment using a sample that is pre-treated and covered with the Er oxide layer is needed to investigate the self-recovery effect.

Enlarged photos of the IMC layer formed after 200 h and 1,500 h immersion in SBLE-25 are shown in Fig. 24. The IMC layer mainly consists of Sn and Fe. Similar IMC layer was also found and identified as $FeSn_2$ in the former studies in Refs. 35 and 36, where corrosion of pure Fe, SUS316, and RAFM (Reduced Activity Ferritic/Martensitic steel) by pure Sn were investigated. The thickness of the IMC layer, $w_{IMC}(t)$, where t is the immersion time, was ~45 μm at t = 200 h (Fig. 24(a)). Interestingly, $w_{IMC}(t)$ did not largely increase even at t = 1,500 h (Fig. 24(b)). Time history of the $w_{IMC}(t)$ is plotted in Fig. 25.

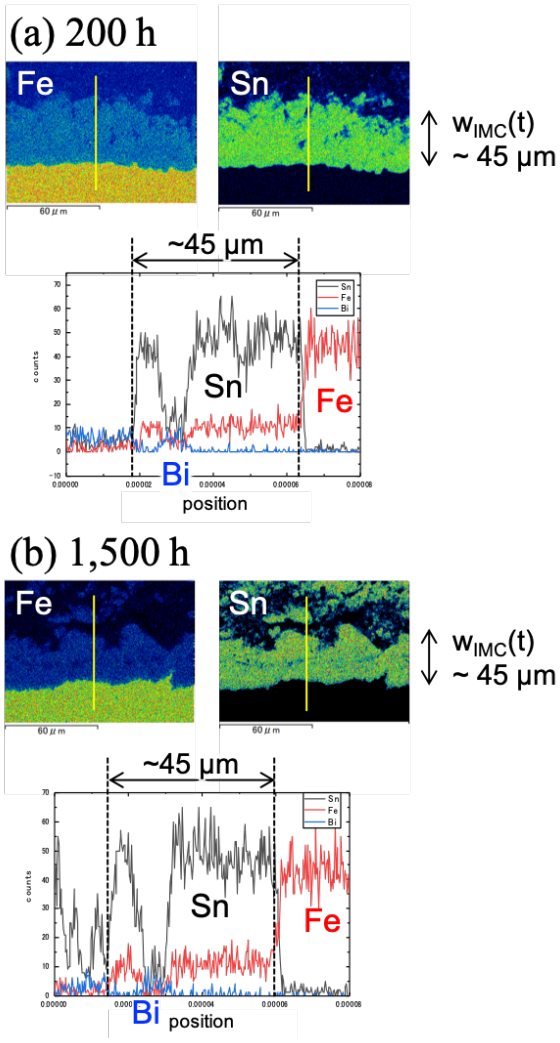

Figure 24. Results of the compositional analysis by EDX on the IMC layer formed on the outer periphery of the sample pipe immersed in SBLE-25 at 400°C for (a) 200 h, and (b) 1,500 h, respectively.

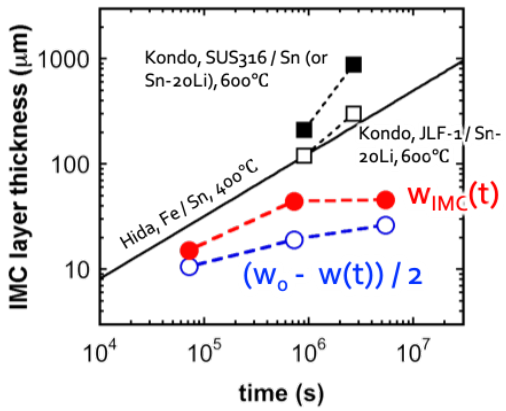

Figure 25. Time trend of the IMC layer thickness, $w_{IMC}(t)$, and the corrosion layer thickness defined by $(w_0 - w(t)) / 2$, together with the former experimental results given by Hida [31] and Kondo [32].

One of the possible explanations on the saturation of $w_{IMC}(t)$ might be that the IMC layer was delaminated in the SBLE-25 due to the rotating motion of the sample pipe. In Fig. 25, also plotted is the corrosion layer thickness defined by $(w_0 - w(t))$ / 2, where $w(t)$ is the thickness between the inner and outer IMC layers (see Fig. 23(b)). As can be seen in Fig. 25, the corrosion layer thickness is smaller than $w_{IMC}(t)$ and not clearly saturate as $w_{IMC}(t)$. If the trend is linearly extended with the immersion time, the corrosion layer thickness will be ~40 μm, more or less, at t = 1 year. This is much lower than the corrosion layer thickness expected for the cases of pure iron, SUS316, and RAFM immersed in pure Sn, given by Hida [35] and Kondo [36], which are also plotted in Fig. 25. In the case of pure iron immersed in pure Sn of 400℃ for one year, the corrosion layer thickness is expected to be as large as ~1 mm. The corrosiveness of SBLE-25 is largely mitigated compared with that of pure tin. This might be related with the reduced chemical activity of tin. Although further investigation to clarify the corrosiveness of FLMs is remained for future studies, the low corrosion rate of ~40 μm/year in the case of SUS304 immersed in SBLE-25 is a preferable result.

5. Summary

Coordinated design of the cartridge-type blanket and the ceramic pebble divertor has been proposed for the helical fusion reactor FFHR-b3. The cartridge-type blanket has been updated to the CARDISTRY-B3 by introducing the slit first wall to increase the manufacturability. Liquid metal oozes from the slit first wall and covers the first wall with the liquid metal surface flow. The helical divertor region is also covered by the liquid metal surface flow and the solid divertor target is not necessary in this design. Simultaneously, the ceramic pebble divertor REVOLVER-D3 has been adopted. Ceramic pebbles dropped to the inboard ergodic layer catch the 70 % of plasma heat load flowing out to the divertor. The ceramic pebbles are mixed with the liquid metal in the pool to exchange its heat and then filtered and circulated again. Screw conveyors are used to circulate the ceramic pebbles and liquid metal. As the working fluid for the CARDISTRY-B3, investigation on the FLM has been started and several candidates of the FLM has been selected. The corrosion experiment of SUS304 using SBLE-25, which is one of the candidates of FLM, has been carried out. SBLE-25 becomes liquified at a low temperature of ~135℃, as expected by a thermodynamic equilibrium calculation code. It has also been found that SBLE-25 can be easily reduced in a hydrogen atmosphere. Corrosiveness of SBLE-25 is largely mitigated compared with pure Sn.

Acknowledgements

This work was supported by the budget of NIFS15UFFF038 and NIFS21UFZG012 of the National Institute for Fusion Science.

References

[1] B. Badger et al., UWMAK-I – A Wisconsin Toroidal Fusion Reactor Design, UWFDM-68 (1973).
[2] M.A. Abdou et al., Fusion Eng. Des. **54** (2001) 181.
[3] S.V. Mirnov et al., J. Nucl. Mater. **196-198** (1992) 45.
[4] R.E. Nygren F.L. Tabarés, Nucl. Mater. Energy 9 (2016) 6.
[5] J. Miyazawa et al., Fusion Eng. Des. **125** (2017) 227.
[6] M. Kondo, Y. Nakajima, Fusion Eng. Des. **88** (2013) 2556.
[7] T. Goto et al., Plasma Fusion Res. **14** (2019) 1405092.
[8] T. Ohgo et al., Plasma Fusion Res. **14** (2019) 3405050.
[9] T. Ohgo et al., Fusion Eng. Des. **165** (2021) 112236.
[10] M. Isobe et al., Nucl. Fusion **40** (2000) 327.
[11] K. Matsumoto et al., Nucl. Fusion **41** (2001) 827.
[12] T. Okui et al., Fusion Technol. **39** (2001) 934.
[13] T. Okui et al., Fusion Eng. Des. **61-62** (2002) 203.
[14] G. Voss et al., Fusion Eng. Des. **81** (2006) 327.
[15] G. Voss et al., Fusion Eng. Des. **83** (2008) 1648.
[16] N. Gierse et al., Nucl. Mater. Energy **2** (2015) 12.
[17] A. Sagara et al., Fusion Eng. Des. **29** (1995) 51.
[18] A. Sagara et al., Fusion Tech. **39** (2001) 753.
[19] A. Sagara et al., Nucl. Fusion **57** (2017) 086046.
[20] T. Goto et al., Plasma Fusion Res. **11** (2016) 2405047.
[21] J. Miyazawa et al., Plasma Fusion Res. **12** (2017) 1405017.
[22] J. Miyazawa et al., Plasma Fusion Res. **14** (2019) 1405163.
[23] J. Miyazawa et al., Nucl. Fusion (accepted).
[24] J. Miyazawa et al., Fusion Eng. Des. **146** (2019) 2233.
[25] A. Komori et al., Fusion Sci. Technol. **58** (2010) 1.
[26] C. Rorres, J. Hydraul. Eng. **126** (2000) 72.
[27] G. Motojima et al., Nucl. Fusion **58** (2018) 014005.
[28] A. Sagara et al., Fusion Eng. Des. **87** (2012) 594.
[29] S. Matsunaga et al., IEEE Trans. Appl. Supercond. **30** (2020) 4601405.
[30] Z. Yao et al., J. Nucl. Mater. **329-333** (2004) 1414.
[31] Z. Yao et al., Fusion Eng. Des. **81** (2006) 951.
[32] T. Chikada et al., Fusion Eng. Des. **82** (2007) 2572.
[33] M. Kondo et al., IAEA-TECDOC-1912 (2020) 157.
[34] C.J. Werner et al., MCNP Version 6.2 Release Notes, LA-UR-18-20808 (Los Alamos National Laboratory, 2018), https://doi.org/10.2172/1419730.
[35] M. Hida and M. Kajihara, Mater. Trans. **53** (2012) 1240.
[36] M. Kondo et al., Fusion Eng. Des. **98-99** (2015) 2003.